CrystEngComm

Dimensional Reduction upon Calcium Incorporation in Cs0.3(Ca0.3Ln0.7)PS4 and Cs0.5(Ca0.5Ln0.5)PS4

Journal:	*CrystEngComm*
Manuscript ID	CE-ART-10-2020-001524.R1
Article Type:	Paper
Date Submitted by the Author:	16-Nov-2020
Complete List of Authors:	Klepov, Vladislav; University of South Carolina, Department of Chemistry and Biochemistry Kocevski, Vancho; Los Alamos National Laboratory, Besmann, Theodore; University of South Carolina, Mechanical Engineering Zur Loye, Hans-Conrad; University of South Carolina, Department of Chemistry and Biochemistry

Dimensional Reduction upon Calcium Incorporation in $Cs_{0.3}(Ca_{0.3}Ln_{0.7})PS_4$ and $Cs_{0.5}(Ca_{0.5}Ln_{0.5})PS_4$

Vladislav V. Klepov,[1] Vancho Kocevski,[2,3] Theodore M. Besmann,[3] and Hans-Conrad zur Loye[1]*

[1]*Department of Chemistry and Biochemistry,* [3]*Department of Mechanical Engineering, University of South Carolina, Columbia, SC, 29208*
[2]*MST-8, Los Alamos National Laboratory, Los Alamos, NM 87545, USA.*
**Corresponding author. E-mail: zurloye@mailbox.sc.edu*

Abstract

Two series of new lanthanide thiophosphates with partial Ca occupancy of the *Ln* sites, $Cs_{0.3}(Ca_{0.3}Ln_{0.7})PS_4$ (*Ln* = Ce, Pr, Nd, Sm, Gd, Tb, and Dy) and $Cs_{0.5}(Ca_{0.5}Ln_{0.5})PS_4$ (*Ln* = Pr, Nd, Sm, Gd, and Tb), were synthesized using a CsI flux and structurally characterized. The first series with an idealized formula of $Cs_{0.3}(Ca_{0.3}Ln_{0.7})PS_4$ crystallizes in the $R\bar{3}m$ space group and belongs to a new structure type that consists of a channel containing $[(Ca_{0.3}Ln_{0.7})PS_4]^{0.3-}$ framework, where the channels are occupied by severely disordered Cs^+ cations. A second new series with formula $Cs_{0.5}(Ca_{0.5}Ln_{0.5})PS_4$ crystallizes in the monoclinic *C*2/*c* space group and exhibits a layered structure consisting of $[(Ca_{0.5}Ln_{0.5})PS_4]^{0.5-}$ layers with Cs^+ cations located between the layers for charge balance. Together with the parent structure type, $LnPS_4$, these three structure types illustrate how the $LnPS_4$ structure changes with Cs^+ cation incorporation, reducing its dimensionality from 3D to 2D. The magnetic properties of $Cs_{0.3}[(Ca_{0.3}Ce_{0.7})PS_4]$ and $Cs_{0.3}[(Ca_{0.3}Pr_{0.7})PS_4]$ were studied and revealed no magnetic transition down to 2 K.

Introduction

A renewed interest in chalcophosphate phases has recently emerged due to their rich structural chemistry and high ion conductivities that are distinct from similar oxide materials. Specifically, lithium and sodium thiophosphate phases have been studied for their unique ion conducting properties,[1–5] while layered thiophosphates that contain 3*d* transition metals show great promise in the design of new 2D materials,[6,7] including magnetically ordering systems.[8,9] Multiple thiophosphate phases exhibit promising optical properties, such as second harmonic generation and luminescence.[10–14] The rich structural chemistry of the chalcophosphates stems from the ability of chalcophosphate groups to condense into more complex structural units, resulting in a large variety of chalcophosphate anions, such as PS_4^{3-},[15–20], $P_2S_7^{4-}$,[21–23] $P_2S_6^{4-}$,[24,25] $P_2S_6^{2-}$,[26,27] etc.,[28–30] with phosphorus in the +4 and +5 oxidation states. This extensive variety of building units represents a unique platform for achieving new crystal structures, although assuming full synthetic control over the structure and the formation of a desired product phase remains challenging. It is therefore desirable to develop a set of general crystal chemical rules that govern the formation of chalcophosphates with which to predict their structures and relate them to the observed properties.

One general trend observed in the formation of lanthanide and actinide chalcophosphates is their structural modularity, which manifests itself in a preferred coordination environment of the metal centers. For example, it is generally found that early lanthanides prefer a nine-fold sulfide coordination environment, while later lanthanides tend to prefer a lower coordination number due to the lanthanide contraction. This trend has revealed itself in the recently reported $Cs_2NaLn(PS_4)_2$ (*Ln* = La–Nd, Sm, Gd–Ho) series,[31] in which there is no apparent structural change throughout the series except for a change in the coordination number of the lanthanide cations from 9 to 8. Despite the change in the coordination number, the topology of the compounds does not change and each lanthanide cation is surrounded by four thiophosphate units, as it is typically observed in lanthanide thiophosphates.[31] While the influence of the lanthanide size on the structure is relatively well studied, there is little information available on how substitutional disorder resulting from placing heterovalent cations on the lanthanide sites impacts the observed structure formation in lanthanide thiophosphates. There are only a handful of elements with a size that is close to that of lanthanide cations, among them Ca^{2+}, which is one that most frequently shares a crystallographic site with a lanthanide cation.[32] This motivated us to study the influence of Ca

incorporation on the resultant structures and elemental compositions of lanthanide thiophosphates.

In this report we describe the results of exploratory crystal growth in the Ln_2S_3–CaS–P_2S_5 system. As alkali halide fluxes proved useful for the synthesis and crystallization of a number of oxide and chalcogenide materials,[33–36] we selected CsI as a flux due to its relatively low melting point, 632 °C.[37–39] Two series of isotypic compounds with different fractions of Ca substitution on the *Ln* sites were obtained, $Cs_{0.3}(Ca_{0.3}Ln_{0.7})PS_4$ (*Ln* = Ce, Pr, Nd, Sm, Gd, Tb, and Dy) and $Cs_{0.5}(Ca_{0.5}Ln_{0.5})PS_4$ (*Ln* = Pr, Nd, Sm, Gd, and Tb), and structurally characterized. The Ca content in the crystallized materials was found to be a function of the Ca content in the reaction mixture for the early lanthanide (Ce–Nd) thiophosphates, while for the remainder of the series, the reaction products consisted of both structure types crystallizing simultaneously in the same crystal growth reaction, regardless of the calcium content of the reaction mixture. By comparing the obtained structures with that of the parent, $LnPS_4$,[40] a structure dimensionality trend was revealed and is discussed herein. In addition, the magnetic and optical properties of $Cs_{0.3}(Ca_{0.3}Ce_{0.7})PS_4$ and $Cs_{0.3}(Ca_{0.3}Pr_{0.7})PS_4$ were investigated and are described.

Experimental

Materials. P_2S_5 (99%, Sigma-Aldrich), CsI (99.9%, Alfa Aesar), CaS (99.9%, Alfa Aesar), CeO_2 (Alfa Aesar, 99.99%), Pr_6O_{11} (Alfa Aesar, 99.99%), Nd_2O_3 (Alfa Aesar, 99.99%), Sm_2O_3 (Alfa Aesar, 99.99%), Gd_2O_3 (Alfa Aesar, 99.99%), Tb_4O_7 (Alfa Aesar, 99.9%), Dy_2O_3 (Alfa Aesar, 99.9%), Ho_2O_3 (Alfa Aesar, 99.99%), and N,N-dimethylformamide (Sigma-Aldrich) were used as received. P_2S_5 and CaS were stored and handled in a glove bag under house nitrogen. Lanthanide sulfides were prepared according to the procedure described in the literature.[41]

Synthesis. $Cs_{0.3}(Ca_{0.3}Ln_{0.7})PS_4$ (*Ln* = Ce, Pr, Nd, Sm, Gd, Tb, and Dy) and $Cs_{0.5}(Ca_{0.5}Ln_{0.5})PS_4$ (*Ln* = Pr, Nd, Sm, Gd, and Tb) were obtained by a reaction of CaS, P_2S_5, and the respective lanthanide sulfide in the molar ratios listed in Table 1 in a CsI flux. For molar ratios of 8:6:1 and 4:4:1, 0.166 mmol of Ln_2S_3 was used to calculate the weight of the other materials, whereas for a 16:8:1 molar ratio, a 0.083 mmol sample of Pr_2S_3 was used. In

all cases, 0.50 g of CsI flux together with the other starting materials were placed into a fused silica tube and sealed under dynamic vacuum. The sealed tubes were placed into a programmable furnace, which was ramped up to 750 °C in one hour, kept at this temperature for 10 hours, cooled to 500 °C in 25 hours at a rate of 10 °C/h and then to room temperature by switching off the furnace. The flux was dissolved in N,N-dimethylformamide and the product was filtered and washed with methanol. The products were found to be moderately moisture sensitive and decompose in humid air in about two days. The crystals of $Cs_{0.3}(Ca_{0.3}Ce_{0.7})PS_4$ and $Cs_{0.3}(Ca_{0.3}Pr_{0.7})PS_4$ were obtained as nearly phase pure samples in a 34 or 44% yield, while the other reactions resulted in mixed phases. Yellow crystals of $Ca_2P_2S_6$ were identified as a major impurity in the samples.[42]

Table 1. $CaS:P_2S_5:Ln_2S_3$ molar ratios used in reactions.

	Ce	Pr	Nd	Sm	Gd	Tb	Dy
$Cs_{0.3}(Ca_{0.3}Ln_{0.7})PS_4$	8:6:1	8:6:1	4:4:1	8:8:1	8:6:1	8:6:1	8:6:1
$Cs_{0.5}(Ca_{0.5}Ln_{0.5})PS_4$	-	16:8:1	8:6:1				

Single Crystal X-ray Diffraction. Single-crystal X-ray diffraction data were collected at 300(2) K on a Bruker D8 QUEST diffractometer equipped with an Incoatec IμS 3.0 microfocus radiation source (MoKα, λ = 0.71073 Å) and a PHOTON II area detector. The crystals were mounted on a microloop using immersion oil. The raw data reduction and absorption corrections were performed using SAINT and SADABS programs.[43,44] Initial structure solutions were obtained with SHELXS-2017 using direct methods and Olex2 GUI.[45] Full-matrix least-square refinements against F^2 were performed with SHELXL software.[46] All the structures were checked for missing symmetry with the Addsym program implemented into PLATON software and no higher symmetry was found.[47] The crystallographic data and results of the diffraction experiments are summarized in Tables 2 and 3.

For $Cs_x(Ca_xLn_{1-x})PS_4$ (*Ln* = Ce, Pr, Nd, Sm, Gd, Tb, Dy), the Ca and *Ln* atoms were found to occupy the same crystallographic position. Both atoms were restrained to fully occupy the site and refined, resulting in a Ca:*Ln* ratio of around 0.30 with no apparent dependence on the *Ln* atom. Although there may be some variability in the compositions, it did not significantly affect the R_1 values, Ca and *Ln* site occupancies in all structures were set

to 0.30 and 0.70, respectively, while the cesium sites were restrained to give a total of 0.30 Cs atoms per formula units to maintain the charge balance. In $Cs_{0.5}(Ca_{0.5}Ln_{0.5})PS_4$, the Ca/*Ln* shared sites were set to 50/50 occupancy to account for the electron density on the site and to maintain charge balance with the fully occupied Cs sites.

Table 2. Crystallographic data for $Cs_{0.3}(Ca_{0.3}Ln_{0.7})PS_4$ (*Ln* = Ce, Pr, Nd, Sm, Gd, Tb, and Dy).

Empirical formula	$Cs_{0.3}(Ca_{0.3}Ln_{0.7})PS_4$						
	Ce	Pr	Nd	Sm	Gd	Tb	Dy
Formula weight	309.19	309.74	312.08	316.35	321.18	322.35	324.86
Temperature/K	300(2)						
Crystal system	Trigonal, 18						
Space group	$R\bar{3}m$						
a/Å	16.5183(3)	16.4968(4)	16.4932(4)	16.4128(3)	16.3458(3)	16.3448(4)	16.3288(4)
c/Å	13.6408(3)	13.5795(3)	13.5289(3)	13.4526(3)	13.4242(3)	13.3425(3)	13.3220(4)
Volume/Å^3	3223.30(14)	3200.47(17)	3187.15(17)	3138.35(13)	3106.21(13)	3086.93(17)	3076.16(18)
ρ_{calc}g/cm^3	2.867	2.893	2.927	3.013	3.091	3.121	3.156
μ/mm^{-1}	7.477	7.845	8.194	9.004	9.868	10.379	10.825
F(000)	2558.0	2570.0	2583.0	2608.0	2633.0	2646.0	2659.0
Crystal size/mm^3	0.06×0.06×0.05	0.10×0.10×0.05	0.05×0.04×0.04	0.05×0.05×0.03	0.10×0.10×0.05	0.03×0.02×0.02	0.02×0.02×0.01
Radiation	MoKα (λ = 0.71073)						
2θ range for data collection/°	6.432–54.878	6.444–54.978	6.452–54.97	6.484–59.988	6.508–54.982	6.516–54.998	4.99–54.992
Index ranges	-21 ≤ h ≤ 21, -21 ≤ k ≤ 21, -17 ≤ l ≤ 17	-21 ≤ h ≤ 21, -21 ≤ k ≤ 21, -17 ≤ l ≤ 17	-21 ≤ h ≤ 21, -21 ≤ k ≤ 21, -17 ≤ l ≤ 17	-22 ≤ h ≤ 23, -23 ≤ k ≤ 23, -18 ≤ l ≤ 18	-21 ≤ h ≤ 21, -21 ≤ k ≤ 21, -17 ≤ l ≤ 17	-21 ≤ h ≤ 21, -21 ≤ k ≤ 21, -17 ≤ l ≤ 16	-21 ≤ h ≤ 20, -21 ≤ k ≤ 21, -17 ≤ l ≤ 17
Reflections collected	37202	68364	32476	30331	62321	30233	23058
Independent reflections	908 [R_{int} = 0.0248, R_{sigma} = 0.0063]	902 [R_{int} = 0.0278, R_{sigma} = 0.0059]	906 [R_{int} = 0.0247, R_{sigma} = 0.0063]	1124 [R_{int} = 0.0274, R_{sigma} = 0.0087]	878 [R_{int} = 0.0267, R_{sigma} = 0.0050]	875 [R_{int} = 0.0243, R_{sigma} = 0.0069]	878 [R_{int} = 0.0355, R_{sigma} = 0.0101]
Data/restraints/parameters	908/1/43	902/1/43	906/1/44	1124/1/43	878/1/43	875/1/43	878/1/43
Goodness-of-fit on F^2	1.138	1.085	1.161	0.980	1.138	1.126	1.140
Final R indexes [I>=2σ (I)]	R_1 = 0.0387, wR_2 = 0.1094	R_1 = 0.0327, wR_2 = 0.0859	R_1 = 0.0330, wR_2 = 0.0922	R_1 = 0.0343, wR_2 = 0.1061	R_1 = 0.0323, wR_2 = 0.0910	R_1 = 0.0298, wR_2 = 0.0878	R_1 = 0.0311, wR_2 = 0.0876
Final R indexes [all data]	R_1 = 0.0388, wR_2 = 0.1095	R_1 = 0.0327, wR_2 = 0.0859	R_1 = 0.0332, wR_2 = 0.0924	R_1 = 0.0352, wR_2 = 0.1075	R_1 = 0.0323, wR_2 = 0.0910	R_1 = 0.0298, wR_2 = 0.0878	R_1 = 0.0327, wR_2 = 0.0897
Largest diff. peak/hole / e Å^{-3}	3.74/-3.95	3.37/-4.62	3.26/-4.44	3.48/-3.56	3.69/-3.7	3.04/-4.25	3.72/-3.72

Table 3. Crystallographic data for $Cs_{0.50}(Ca_{0.50}Ln_{0.50})PS_4$ (*Ln* = Pr, Nd, Sm, Gd, Tb, and Dy).

Empirical formula	$Cs_{0.50}(Ca_{0.50}Ln_{0.50})PS_4$					
	Pr	Nd	Sm	Gd	Tb	Dy
Formula weight	316.16	317.83	320.88	324.33	325.17	326.96
Temperature/K	300(2)					
Crystal system, *Z*	Monoclinic, 8					
Space group	*C*2/*c*					
a/Å	9.2095(2)	9.1970(2)	9.1778(3)	9.1603(2)	9.1479(4)	9.1378(2)
b/Å	9.2341(2)	9.2233(2)	9.2037(3)	9.1898(2)	9.1800(4)	9.1727(2)
c/Å	16.7221(4)	16.7149(4)	16.6857(5)	16.6882(4)	16.6874(7)	16.6704(4)
β/°	103.9463(8)	103.8709(8)	103.7780(13)	103.6865(8)	103.6882(15)	103.6778(8)
Volume/Å^3	1380.15(5)	1376.52(5)	1368.88(8)	1364.94(5)	1361.57(10)	1357.66(5)
ρ_{calc}g/cm^3	3.043	3.067	3.114	3.157	3.173	3.199
μ/mm^{-1}	7.897	8.15	8.692	9.274	9.62	9.942
F(000)	1168	1172	1180	1188	1192	1196
Crystal size/mm^3	0.04×0.03×0.01	0.05×0.05×0.02	0.06×0.04×0.01	0.06×0.05×0.01	0.08×0.06×0.03	0.24×0.06×0.06
Radiation	MoKα (λ = 0.71073)					
2θ range for data collection/°	6.344–64.974	5.02–56.984	5.028–59.99	6.372–59.976	5.024–54.98	6.386–59.998
Index ranges	-12 ≤ h ≤ 13, -13 ≤ k ≤ 13, -25 ≤ l ≤ 25	-12 ≤ h ≤ 11, -12 ≤ k ≤ 12, -22 ≤ l ≤ 22	-12 ≤ h ≤ 12, -12 ≤ k ≤ 12, -23 ≤ l ≤ 23	-12 ≤ h ≤ 12, -12 ≤ k ≤ 12, -23 ≤ l ≤ 23	-11 ≤ h ≤ 11, -11 ≤ k ≤ 11, -21 ≤ l ≤ 21	-12 ≤ h ≤ 12, -12 ≤ k ≤ 12, -23 ≤ l ≤ 23
Reflections collected	26261	17462	19807	35177	25062	49642
Independent reflections	2487 [R_{int} = 0.0313, R_{sigma} = 0.0148]	1748 [R_{int} = 0.0545, R_{sigma} = 0.0215]	1989 [R_{int} = 0.0360, R_{sigma} = 0.0185]	1975 [R_{int} = 0.0287, R_{sigma} = 0.0105]	1562 [R_{int} = 0.0356, R_{sigma} = 0.0141]	1972 [Rint = 0.0417, Rsigma = 0.0134]
Data/restraints/parameters	2487/0/60	1748/0/60	1989/0/60	1975/0/60	1562/0/60	1972/0/60
Goodness-of-fit on F^2	1.116	1.109	1.098	1.039	1.14	1.086
Final R indexes [I>=2σ (I)]	R_1 = 0.0267, wR_2 = 0.0631	R_1 = 0.0250, wR_2 = 0.0661	R_1 = 0.0231, wR_2 = 0.0526	R_1 = 0.0190, wR_2 = 0.0403	R_1 = 0.0311, wR_2 = 0.0743	R1 = 0.0237, wR2 = 0.0521
Final R indexes [all data]	R_1 = 0.0287, wR_2 = 0.0642	R_1 = 0.0259, wR_2 = 0.0668	R_1 = 0.0247, wR_2 = 0.0534	R_1 = 0.0192, wR_2 = 0.0404	R_1 = 0.0313, wR_2 = 0.0744	R1 = 0.0238, wR2 = 0.0522
Largest diff. peak/hole / e Å^{-3}	1.19/-1.06	1.48/-0.95	0.88/-1.00	0.93/-1.11	1.04/-0.96	0.84/-1.44

Powder X-ray Diffraction. Powder X-ray diffraction (PXRD) data for phase identification were collected on polycrystalline samples ground from single crystals (Figures S1 and S2). Data were collected on a Bruker D2 PHASER diffractometer using Cu Kα radiation over a 2θ range 10–40° with a step size of 0.02°.

Energy-Dispersive Spectroscopy (EDS). EDS was performed on single crystal products using a Tescan Vega-3 SEM equipped with a Thermo EDS attachment. The SEM was operated in the low-vacuum mode. Crystals were mounted on an SEM stub with carbon tape and analyzed using a 20 kV accelerating voltage and an 80 s accumulation time. The results of EDS confirm the presence of elements found by single-crystal X-ray diffraction (Figures S3-S11 and Table S1).

Optical Properties. UV–Vis spectra for $Cs_{0.3}(Ca_{0.3}Ce_{0.7})PS_4$ and $Cs_{0.3}(Ca_{0.3}Pr_{0.7})PS_4$ were recorded using a Perkin Elmer Lambda 35 UV/Visible scanning spectrophotometer used in the diffuse reflectance mode and equipped with an integrating sphere (Figures S12 and S13). Diffuse reflectance spectra were recorded in the 200–900 nm range converted to absorbance using the Kubelka–Munk function. Fluorescence measurements were performed on a sample of $Cs_{0.3}[(Ca_{0.3}Ce_{0.7})PS_4]$ using a PerkinElmer LS55 luminescence spectrometer (Figure S15).

Magnetism. Magnetic property measurements were performed using a Quantum Design MPMS 3 SQUID magnetometer. Zero-field-cooled (ZFC) magnetic susceptibility measurements were performed from 2 to 300 K in an applied field of 0.1 T. The raw data were corrected for radial offset and sample shape effects according to the method described by Morrison and zur Loye.[48]

Crystal Chemical Calculations. Crystal structure analysis was performed using the TOPOS 4.0 software package.[49,50] The method of intersecting spheres was employed for determining the coordination number using the AutoCN program.[51] Dirichlet and ADS programs were employed for Voronoi-Dirichlet polyhedra construction and topological analysis, respectively. The standard structure simplification procedure was employed to obtain the underlying nets of the compounds.[52]

First-Principles Calculations. First-principles calculations were performed using density functional theory (DFT) with the Vienna Ab-initio Package (VASP) planewave code,[53,54] generalized gradient approximation of Perdew, Burke and Ernzerhof (PBE),[55] and projector augmented wave (PAW) method.[56,57] The Ca, Cs, P, and S valence electron configurations considered for construction of PAW potentials were $3s^23p^64s^2$, $5s^25p^66s^1$, $3s^23p^3$, and $3s^23p^4$,

respectively. For the rare-earth elements Ce_3 and Pr_3 pseudopotentials from the VASP distribution were used. These potentials were chosen because other rare-earth pseudopotentials from the VASP distribution exhibited energy convergence issues. To model the partial occupancy of the Cs and *Ln*(Ca) sites (*Ln* = Ce, Pr) for both $Cs_{0.3}(Ca_{0.3}Ln_{0.7})PS_4$ and $Cs_{0.5}(Ca_{0.5}Ln_{0.5})PS_4$, the Cs and Ca sites were chosen so they are nearest neighbors and furthest apart from their own type Cs and Ca, respectively, which ultimately lowers the symmetry of the structure. Spin-polarized calculations were performed, with 520 eV cut-off energy for the plane wave basis set, 10^{-6} eV energy convergence criteria and 3×3×4 and 5×5×4 *k*-point meshes for $Cs_{0.3}(Ca_{0.3}Ln_{0.7})PS_4$ and $Cs_{0.5}(Ca_{0.5}Ln_{0.5})PS_4$. The ground state geometries at 0 K were optimized by relaxing the cell volume, atomic positions, and cell symmetry until the maximum force on each atom is less than 0.01 eV/Å. During the geometry optimization each of the studied compounds relaxed to a state with 0 μ_B net magnetic moment.

Results and Discussion

Synthesis. The synthesis of all compounds was achieved by reacting an excess of calcium sulfide with Ln_2S_3 and P_2S_5 in a CsI flux. For *Ln* = Ce, only the $Cs_{0.3}[(Ca_{0.3}Ce_{0.7})PS_4$ composition was obtained, and adding more CaS to the reaction did not lead to the formation of a $Cs_{0.5}(Ca_{0.5}Ln_{0.5})PS_4$ phase. For *Ln* = Pr, the formation of $Cs_{0.5}(Ca_{0.5}Pr_{0.5})PS_4$ with a higher Ca content was only observed when a 8 : 1 Ca : Pr molar ratio was used in the synthesis, while a lower molar ratio of 4 : 1, under the same reaction conditions, resulted in $Cs_{0.3}(Ca_{0.3}Pr_{0.7})PS_4$. Likewise, an eight-fold excess of Ca in the reaction mixture led to the formation of the $Cs_{0.5}(Ca_{0.5}Nd_{0.5})PS_4$ phase, while a smaller Ca content in the reaction mixture favored the formation of $Cs_{0.3}(Ca_{0.3}Nd_{0.7})PS_4$. For the remainder of the series, both compositions are always found in the product mixture and both can be isolated from the same reaction when using a 4:1 Ca:*Ln* molar ratio, indicating that both phases have similar stabilities under these reaction conditions.

Crystal structure of $Cs_x(Ca_xLn_{1-x})PS_4$ (x ≈ 0.3; *Ln* = Ce, Pr, Nd, Sm, Gd, Tb, Dy). All compounds crystallize in the $R\bar{3}m$ space group and consist of a $[(Ca_{0.3}Ln_{0.7})PS_4]^{0.3-}$ framework containing channels that are occupied by the Cs^+ cations. The underlying net of the framework belongs to a 4,4-connected **ptr** topological type as identified by the TOPOS software package.[52]

As *Ln* and Ca atoms have similar ionic radii, they share a single 18f Wyckoff position with a C_2 site symmetry. Both atoms form *Ln*(Ca)S_8 coordination polyhedra in the shape of a distorted tetragonal antiprism. The *Ln*(Ca)–S bond distances change consistently with the *Ln* cation size, decreasing from 2.9524(14)–2.9742(12) Å for Ce(Ca)–S to 2.9041(15)–2.9412(4) Å for Dy(Ca)–S. Each *Ln*(Ca) site is connected to four tetrahedrally arranged thiophosphate groups, which is typical for lanthanide and uranium thiophosphates.[31] Each thiophosphate group is connected to four *Ln*(Ca) sites, forming a nearly planar fragment. The P–S bond lengths are within a narrow range of 2.021(3)–2.057(3) Å, which is in good agreement with previously reported values.[58-60] The single crystallographic phosphorus atom occupies a 18h Wyckoff position with a C_s site symmetry, resulting in a 1:1 *Ln*(Ca) : PS_4 molar ratio. Since a *Ln*(Ca) site has a total charge of 2.7, the remainder of the negative charge from the thiophosphate groups is balanced by the Cs cations that occupy the channels in the $[(Ca_{0.3}Ln_{0.7})PS_4]^{0.3-}$ framework. The Cs atoms partially occupy several positions throughout the channels, SC XRD data show extremely elongated thermal ellipsoids for them indicating a "smeared" electron density throughout the channels (Figure 1). Significant disorder is indicative of virtually free movement of the Cs^+ cations along the channels, suggesting the existence of low thermal barriers that can be overcome in the temperature range between room temperature and the reaction temperature (750 °C) and, furthermore, that all potential crystallographic sites have virtually the same energies. To confirm this, the total energies as a function of the Cs site occupancy were calculated. The energy barriers for the Cs^+ cation movement along the channels do not exceed 1.14 kJ/mol, which is consistent with the lack of apparent site preference for the Cs^+ cations.

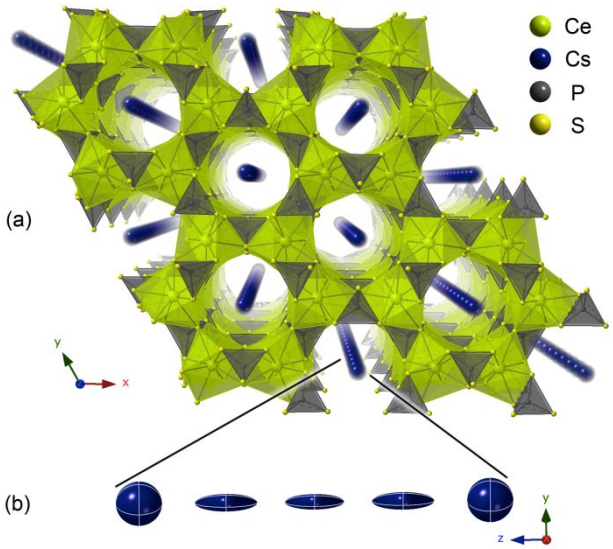

Figure 1. (a) View on the structure of $Cs_{0.3}[(Ca_{0.3}Pr_{0.7})PS_4]$ along the *c* axis and (b) Cs atom thermal ellipsoids showing their disorder along the channels.

$Cs_{0.5}(Ca_{0.5}Ln_{0.5})PS_4$ (*Ln* = Pr, Nd, Sm, Gd, Tb, Dy). All six compounds crystallize in the monoclinic *C*2/*c* space group. The increase in the Cs content results in a dimensional reduction to 2D with the Cs cations located between layers rather than within channels as in $Cs_{0.3}[(Ca_{0.3}Ln_{0.7})PS_4]$. All $Cs_{0.5}(Ca_{0.5}Ln_{0.5})PS_4$ compositions contain $[(Ca_{0.5}Ln_{0.5})PS_4]^{0.5-}$ layers with **sql** topology that are connected into a 3D structure by coulombic interactions with the Cs cations. Unlike in $Cs_x(Ca_xLn_{1-x})PS_4$ ($x \approx 0.3$), the compositions of the crystals do not vary, and all six compounds have Cs, Ca, and *Ln* in an exact 1:1:1 ratio.

Ln and Ca atoms share a single crystallographic site with a 50:50 occupancy and form coordination polyhedra in the shape of a bicapped trigonal prism (Figure 2). The six bonds with the sulfur atoms that occupy the vertices of the trigonal prism are much shorter, 2.8010(8) and 2.9544(8) Å, than the bonds with the capping atoms, 3.3736(13) and 3.4112(13) Å. Like other lanthanide thiophosphates, each Ca/*Ln* site is tetrahedrally surrounded by four thiophosphate groups. Each of the thiophosphate groups is connected to four Ca/*Ln* coordination polyhedra to form the $[(Ca_{0.5}Ln_{0.5})PS_4]^{0.5-}$ layers. The thiophosphate groups form tetrahedra with the P–S bond lengths ranging from 2.0136(10) to 2.0537(11) Å. Unlike $Cs_{0.3}(Ca_{0.3}Ln_{0.7})PS_4$, the Cs atoms in $Cs_{0.5}(Ca_{0.5}Ln_{0.5})PS_4$ fully occupy sites in the interlayer space, exhibiting no compositional or positional variation across the series.

Topological analysis. $Cs_{0.3}[(Ca_{0.3}Ln_{0.7})PS_4]$ and $Cs_{0.5}[(Ca_{0.5}Ln_{0.5})PS_4]$ are related to the $LnPS_4$ by partial replacement of *Ln* with Ca and the incorporation of Cs cations for charge balance.[40] Given similar coordination preferences of the Ca and *Ln* atoms in these structures, one can expect that these compounds have similar cation topologies. In all three structure types, the underlying nets are based on two types of 4-coordinated nodes corresponding to *Ln* sites and PS_4 groups (Figure 3). However, a 1:1 combination of these 4-coordinated nodes results in three distinct topologies due to the incorporation of Cs cations in the structures. The underlying nets in both $PrPS_4$ and $Cs_{0.3}[(Ca_{0.3}Ln_{0.7})PS_4]$ are 3-periodic and have **pts** and **ptr** topologies, respectively. Further Ca and Cs incorporation results in a 2-periodic **sql** topology for the underlying net in $Cs_{0.5}[(Ca_{0.5}Ln_{0.5})PS_4]$. While dimensional reduction is commonly observed when alkali cations are incorporated into a structure,[61] it usually results in a change in the metal cation to anion ratio.[62] The title compounds provide a rather rare illustration of this effect solely as a function of an alkali cation fraction, with the identical Ca/*Ln* : PS_4 cation to anion ratio.

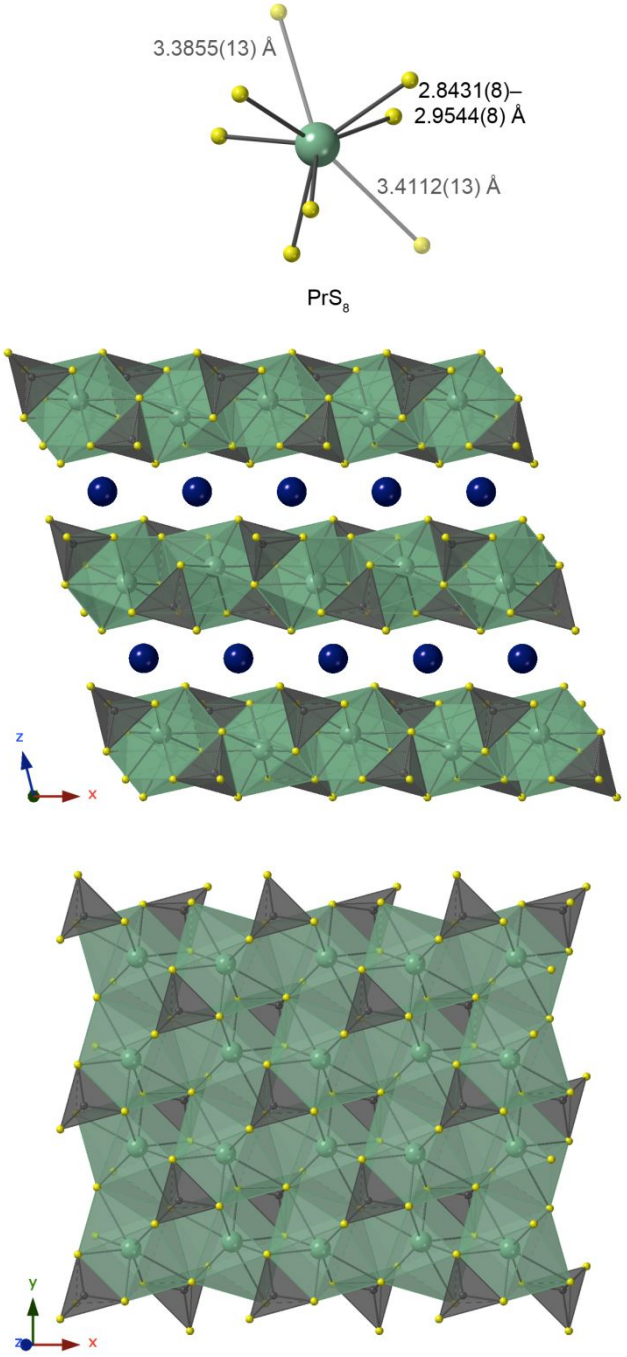

Figure 2. (top) PrS_8 coordination polyhedron, (middle) a view along the *b* axis, and (bottom) a view on a $[(Ca_{0.5}Pr_{0.5})PS_4]^{0.5-}$ layer in the structure of $Cs_{0.5}[(Ca_{0.5}Pr_{0.5})PS_4]$.

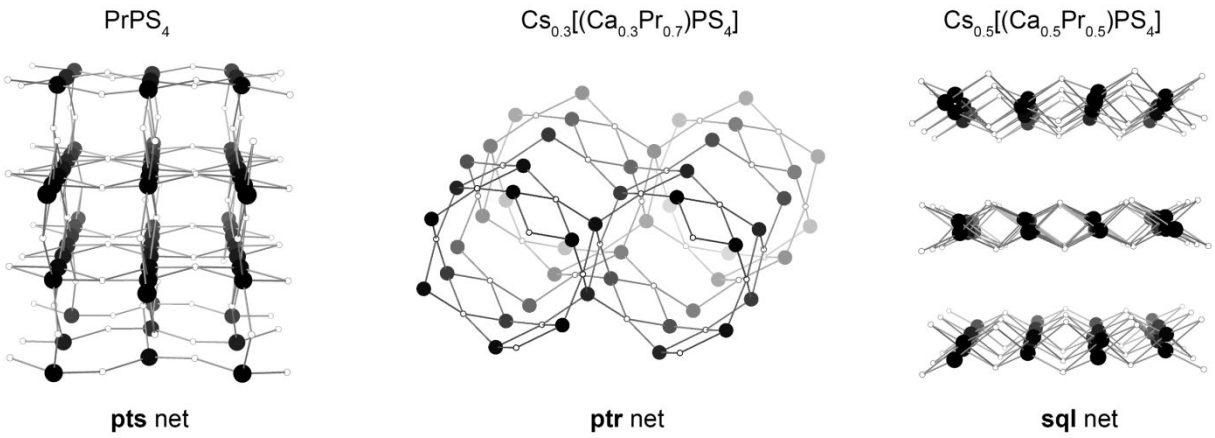

Figure 3. Cation topology of the $[(Ca_xPr_{1-x})PS_4]^{x-}$ frameworks in the structures of (left) $PrPS_4$, (middle) $Cs_{0.3}[(Ca_{0.3}Pr_{0.7})PS_4]$, and (right) $Cs_{0.5}[(Ca_{0.5}Pr_{0.5})PS_4]$.

Magnetic properties. The magnetic properties of $Cs_{0.3}(Ca_{0.3}Ce_{0.7})PS_4$ and $Cs_{0.3}(Ca_{0.3}Pr_{0.7})PS_4$ were determined by measuring magnetic susceptibility *vs*. temperature. Due to the large distances between the lanthanide ions in both structures and partial site occupancy by Ca on the Ce and Pr sites, both compounds reveal no clear magnetic transitions in χ *vs*. *T* plots (Figure 4). The results were fitted to the Curie-Weiss law over the range of 100 to 300 K (Figure 4) to derive effective magnetic moments and Weiss constants for the samples of both compounds. $Cs_{0.3}(Ca_{0.3}Ce_{0.7})PS_4$ has an effective moment of 2.10 μ_B/Ce atom, which is lower than the 2.54 μ_B/Ce atom that was calculated taking spin-orbit coupling into account.[31] Similarly, the effective magnetic moment of Pr atoms in $Cs_{0.3}(Ca_{0.3}Ce_{0.7})PS_4$, 3.23 μ_B/Pr atom, is appreciably lower that the calculated spin-orbit coupling value of 3.58 μ_B/Pr atom. The lower moment is consistent with the fact that both samples contained a small $Ca_2P_2S_6$ impurity that could not be physically or chemically removed, which decreased the mass of the magnetic component in the sample (Figures S1 and S2). Nonetheless, it is clear that the overall magnetic behavior of the samples is paramagnetic, as seen in analogous Ce and Pr thiophosphates.[20,63]

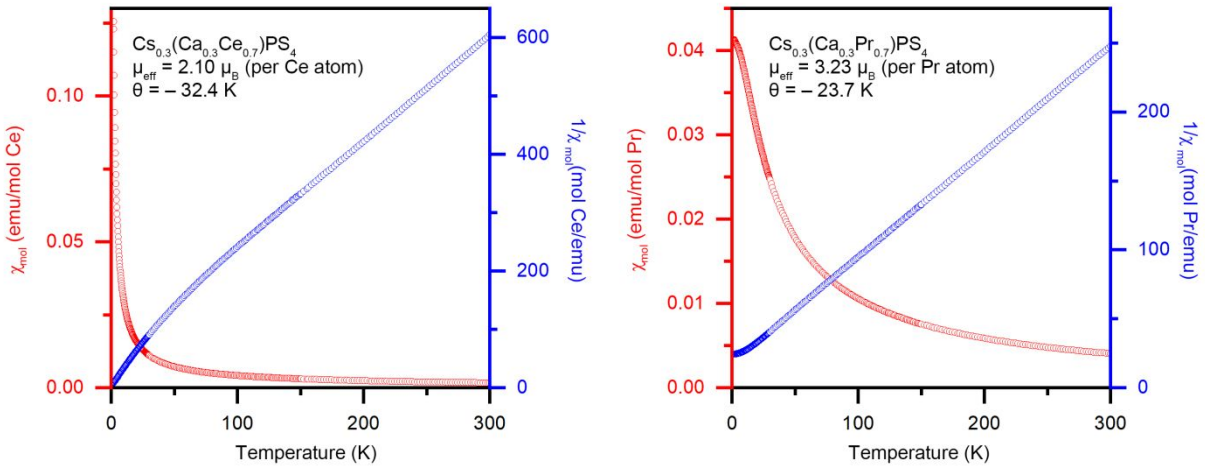

Figure 4. Magnetic susceptibility plots for samples of $Cs_{0.3}(Ca_{0.3}Ce_{0.7})PS_4$ and $Cs_{0.3}(Ca_{0.3}Pr_{0.7})PS_4$.

Optical and electronic properties. UV-vis spectra of $Cs_{0.3}(Ca_{0.3}Ce_{0.7})PS_4$ and $Cs_{0.3}(Ca_{0.3}Pr_{0.7})PS_4$ were collected and the band gap was calculated by linear fit of the absorption onset using Tauc plots (Figure S12 and S13). In the spectrum of $Cs_{0.3}(Ca_{0.3}Pr_{0.7})PS_4$, the peaks in 2.0–2.2 and 2.4–2.8 eV regions correspond to characteristic *f-f* transitions (Figure S13). The direct band gaps are found to be 2.51(6) and 3.12(8) eV for *Ln* = Ce and Pr, respectively, and agree well with the previously reported values for lanthanide thiophosphates.[20] The calculated densities of states (DOS) show a band gap of 2.30 and 2.37 eV for Ce and Pr (Figure 5), agreeing well with the experimental data. Also, $Cs_{0.3}(Ca_{0.3}Ce_{0.7})PS_4$ and $Cs_{0.3}(Ca_{0.3}Pr_{0.7})PS_4$ have very similar DOS, where the top of the valence band is dominated by S states, while the bottom of the conduction band by Ce/Pr states, with some mixture of S and P states. Calculated DOS for $Cs_{0.5}(Ca_{0.5}Pr_{0.5})PS_4$ were found to be similar DOS and to also have a similar band gap of 2.35 eV (Figure S14), indicating no significant difference in their electronic structure.

As $Cs_{0.3}(Ca_{0.3}Ce_{0.7})PS_4$ showed visible yellow-green luminescence under a UV lamp, its photoluminescence emission and excitation spectra were collected. The excitation spectrum (Figure S15) was collected 519 nm and exhibits two maxima. The most intense peak at 415 nm was selected for collecting the emission data. The emission spectrum exhibits a single broad peak with a maximum at 519 nm, which agrees well with a $5d^1 \rightarrow {}^2F_{5/2}$ transition at 510 nm in a previously reported $Ce_6Si_4S_{17}$.[64]

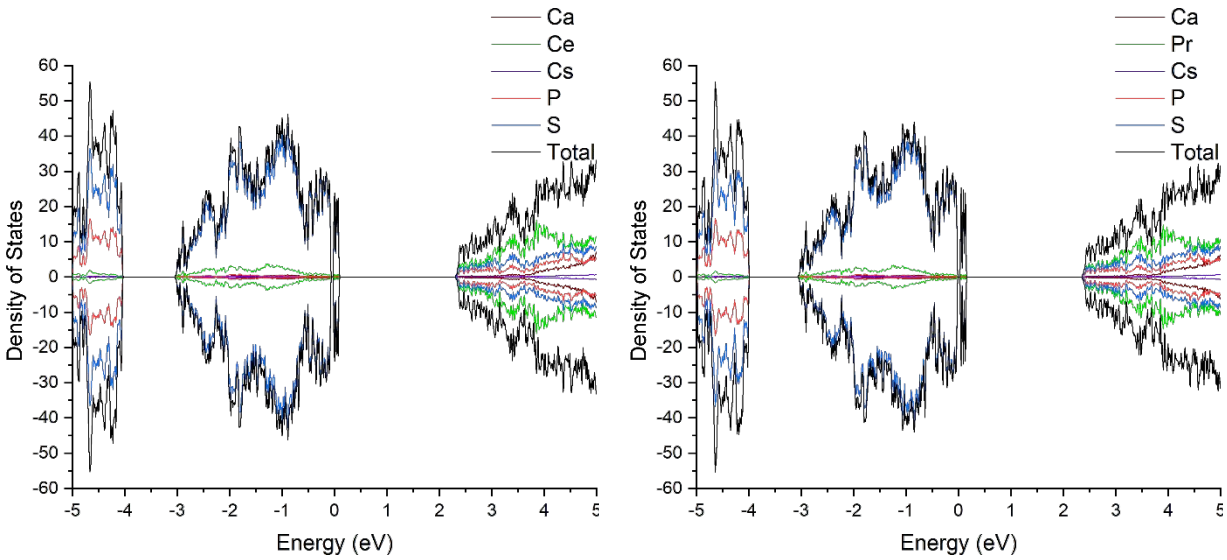

Figure 5. Density of states plots for (left) $Cs_{0.3}(Ca_{0.3}Ce_{0.7})PS_4$ and (right) $Cs_{0.3}(Ca_{0.3}Pr_{0.7})PS_4$.

Conclusions

Two series of lanthanide thiophosphates with *Ln*(Ca) mixed sites in their structures, $Cs_{0.3}(Ca_{0.3}Ln_{0.7})PS_4$ (*Ln* = Ce, Pr, Nd, Sm, Gd, Tb, and Dy) and $Cs_{0.5}(Ca_{0.5}Ln_{0.5})PS_4$ (*Ln* = Pr, Nd, Sm, Gd, and Tb), were synthesized and characterized. The Ca content in the reported phases is a function of a size ratio between the Ca and the *Ln* cations. While the larger lanthanide, Ce, formed only the $Cs_{0.3}(Ca_{0.3}Ce_{0.7})PS_4$ phase, the $Cs_{0.5}(Ca_{0.5}Ln_{0.5})PS_4$ phases form more readily starting from *Ln* = Pr. Similar to previously reported lanthanide thiophosphates $LnPS_4$, the $Cs_{0.3}(Ca_{0.3}Ln_{0.7})PS_4$ structure type is based on a framework containing Cs occupied channels in which their electron density is effectively "smeared" throughout the channels in the framework. Further increase of Ca and Cs content in $Cs_{0.5}(Ca_{0.5}Ln_{0.5})PS_4$ results in dimensional reduction to a layered compound with a **sql** layer topology. Magnetic susceptibility measurements of $Cs_{0.3}(Ca_{0.3}Ce_{0.7})PS_4$ and $Cs_{0.3}(Ca_{0.3}Pr_{0.7})PS_4$ showed no apparent magnetic transitions down to 2 K. Effective magnetic moments of 2.10 and 3.24 μ_B/Ln^{3+} for Ce and Pr, respectively, were derived from Curie-Weiss law and are slightly smaller than the calculated spin-orbit values of 2.54 and 3.58 μ_B/Ln^{3+}.

Acknowledgment

The authors acknowledge financial support from the US Department of Energy, Office of Basic Energy Sciences, Division of Materials Sciences and Engineering under award DE-

SC0018739. This research used computational resources provided by the National Energy Research Scientific Computing Center (NERSC).

Supporting Information

Crystallographic data, EDS results, PXRD patterns, UV-vis spectra, fluorescence spectra (PDF). Further details of the crystal structure investigations may be obtained from the joint CCDC/FIZ Karlsruhe online deposition service: https://www.ccdc.cam.ac.uk/structures/ by quoting the deposition numbers CSD 2038458-2038470.

References

(1) Bachman, J. C.; Muy, S.; Grimaud, A.; Chang, H.-H.; Pour, N.; Lux, S. F.; Paschos, O.; Maglia, F.; Lupart, S.; Lamp, P.; Giordano, L.; Shao-Horn, Y. Inorganic Solid-State Electrolytes for Lithium Batteries: Mechanisms and Properties Governing Ion Conduction. *Chem. Rev.* **2016**, *116* (1), 140–162. https://doi.org/10.1021/acs.chemrev.5b00563.

(2) Janek, J.; Zeier, W. G. A Solid Future for Battery Development. *Nat. Energy* **2016**, *1* (9). https://doi.org/10.1038/nenergy.2016.141.

(3) Dietrich, C.; Weber, D. A.; Culver, S.; Senyshyn, A.; Sedlmaier, S. J.; Indris, S.; Janek, J.; Zeier, W. G. Synthesis, Structural Characterization, and Lithium Ion Conductivity of the Lithium Thiophosphate $Li_2P_2S_6$. *Inorg. Chem.* **2017**, *56* (11), 6681–6687. https://doi.org/10.1021/acs.inorgchem.7b00751.

(4) Bernges, T.; Culver, S. P.; Minafra, N.; Koerver, R.; Zeier, W. G. Competing Structural Influences in the Li Superionic Conducting Argyrodites $Li_6PS_{5-x}Se_xBr$ ($0 \leq x \leq 1$) upon Se Substitution. *Inorg. Chem.* **2018**, *57* (21), 13920–13928. https://doi.org/10.1021/acs.inorgchem.8b02443.

(5) Neuberger, S.; Culver, S. P.; Eckert, H.; Zeier, W. G.; Schmedt auf der Günne, J. Refinement of the Crystal Structure of $Li_4P_2S_6$ Using NMR Crystallography. *Dalton Trans.* **2018**, *47* (33), 11691–11695. https://doi.org/10.1039/C8DT02619J.

(6) Brec, R. Review on Structural and Chemical Properties of Transition Metal Phosphorus Trisulfides MPS_3. In *Intercalation in Layered Materials*; Dresselhaus, M. S., Ed.; NATO ASI Series; Springer US: Boston, MA, 1986; Vol. 148, pp 93–124. https://doi.org/10.1007/978-1-4757-5556-5_4.

(7) Nicolosi, V.; Chhowalla, M.; Kanatzidis, M. G.; Strano, M. S.; Coleman, J. N. Liquid Exfoliation of Layered Materials. *Science* **2013**, *340* (6139), 1226419–1226419. https://doi.org/10.1126/science.1226419.

(8) Joy, P. A.; Vasudevan, S. Magnetism in the Layered Transition-Metal Thiophosphates MPS_3 (*M* = Mn, Fe, and Ni). *Phys. Rev. B* **1992**, *46* (9), 5425–5433. https://doi.org/10.1103/PhysRevB.46.5425.

(9) Susner, M. A.; Chyasnavichyus, M.; McGuire, M. A.; Ganesh, P.; Maksymovych, P. Metal Thio- and Selenophosphates as Multifunctional van Der Waals Layered Materials. *Adv. Mater.* **2017**, *29* (38), 1602852. https://doi.org/10.1002/adma.201602852.

(10) Gauthier, G.; Jobic, S.; Boucher, F.; Macaudière, P.; Huguenin, D.; Rouxel, J.; Brec, R. $CePS_4$ Electronic Structure and Optical Properties. *Chem. Mater.* **1998**, *10* (9), 2341–2347. https://doi.org/10.1021/cm980711k.

(11) Gauthier, G.; Jobic, S.; Brec, R.; Rouxel, J. $K_3CeP_2S_8$: A New Cerium Thiophosphate with One-Dimensional Anionic Chains. *Inorg. Chem.* **1998**, *37* (10), 2332–2333. https://doi.org/10.1021/ic980091p.

(12) Misuryaev, T. V.; Murzina, T. V.; Aktsipetrov, O. A.; Sherstyuk, N. E.; Cajipe, V. B.; Bourdon, X. Second Harmonic Generation in the Lamellar Ferrielectric $CuInP_2S_6$. *Solid State Comm.* **2000**, *115* (11), 605–608. https://doi.org/10.1016/S0038-1098(00)00257-X.

(13) Gauthier, G.; Klur, Y.; Pourpoint, A.; Jobic, S.; Ouvrard, G.; Brec, R.; Huguenin, D.; Macaudière, P. Absence of Chromatic Effect: Crystal Relaxation around CeIII in $Y_{1-x}Ce_xPS_4$ ($0 \leq x \leq 1$). *International J. Inorg. Mater.* **2000**, *2* (6), 717–722. https://doi.org/10.1016/S1466-6049(00)00076-3.

(14) Fan, Y.-H.; Jiang, X.-M.; Liu, B.-W.; Li, S.-F.; Guo, W.-H.; Zeng, H.-Y.; Guo, G.-C.; Huang, J.-S. Phase Transition and Second Harmonic Generation in Thiophosphates $Ag_2Cd(P_2S_6)$ and $AgCd_3(PS_4)S_2$ Containing Two Second-Order Jahn–Teller Distorted Cations. *Inorg. Chem.* **2017**, *56* (1), 114–124. https://doi.org/10.1021/acs.inorgchem.6b01016.

(15) Jin, G. B.; Skanthakumar, S.; Haire, R. G.; Soderholm, L.; Ibers, J. A. Neptunium Thiophosphate Chemistry: Intermediate Behavior between Uranium and Plutonium. *Inorg. Chem.* **2011**, *50* (19), 9688–9695. https://doi.org/10.1021/ic201493w.

(16) Babo, J.-M.; Diefenbach, K.; Albrecht-Schmitt, T. E. $A_6U_3Sb_2P_8S_{32}$ (A = Rb, Cs): Quinary Uranium(IV) Thiophosphates Containing the $[Sb(PS_4)_3]^{6-}$ Anion. *Inorg. Chem.* **2014**, *53* (7), 3540–3545. https://doi.org/10.1021/ic403044x.

(17) Mesbah, A.; Prakash, J.; Beard, J. C.; Lebègue, S.; Malliakas, C. D.; Ibers, J. A. Syntheses, Crystal Structures, Optical and Theoretical Studies of the Actinide Thiophosphates $SrU(PS_4)_2$, $BaU(PS_4)_2$, and $SrTh(PS_4)_2$. *Inorg. Chem.* **2015**, *54* (6), 2970–2975. https://doi.org/10.1021/acs.inorgchem.5b00071.

(18) Dressel, C. B.; Klein, W.; Fässler, T. F. $CuTiPS_5$ - A New Structure Type with a Corrugated Layered Network Structure: $CuTiPS_5$ - A New Structure Type with a Corrugated Layered Network Structure. *Z. Anorg. Allg. Chem.* **2017**, *643* (23), 1814–1817. https://doi.org/10.1002/zaac.201700178.

(19) Ovsyannikov, S. V.; Morozova, N. V.; Korobeinikov, I. V.; Haborets, V.; Yevych, R.; Vysochanskii, Y.; Shchennikov, V. V. Tuning the Electronic and Vibrational Properties of $Sn_2P_2Se_6$ and $Pb_2P_2S_6$ Crystals and Their Metallization under High Pressure. *Dalton Trans.* **2017**, *46* (13), 4245–4258. https://doi.org/10.1039/C6DT03854A.

(20) Klepov, V. V.; Breton, L. S.; Pace, K. A.; Kocevski, V.; Besmann, T. M.; Zur Loye, H.-C. Size-Driven Stability of Lanthanide Thiophosphates Grown from an Iodide Flux. *Inorg. Chem.* **2019**, *58* (9), 6565–6573. https://doi.org/10.1021/acs.inorgchem.9b00806.

(21) Goh, E.-Y.; Kim, E.-J.; Kim, S.-J. Structure Modification on Quaternary Rare Earth Thiophosphates: $NaYbP_2S_6$, $NaSmP_2S_6$, and $KSmP_2S_7$. *J. Solid State Chem.* **2001**, *160* (1), 195–204. https://doi.org/10.1006/jssc.2001.9222.

(22) Gutzmann, A.; Näther, C.; Bensch, W. $CsVP_2S_7$. *Acta Crystallogr. E Struct. Rep. Online* **2005**, *61* (1), i6–i8. https://doi.org/10.1107/S1600536804031150.

(23) Neuhausen, C.; Hatscher, S. T.; Panthöfer, M.; Urland, W.; Tremel, W. Comprehensive Uranium Thiophosphate Chemistry: Framework Compounds Based on Pseudotetrahedrally Coordinated Central Metal Atoms: Comprehensive Uranium Thiophosphate Chemistry. *Z. Anorg. Allg. Chem.* **2013**, *639* (15), 2836–2845. https://doi.org/10.1002/zaac.201300300.

(24) Chan, B. C.; Hess, R. F.; Feng, P. L.; Abney, K. D.; Dorhout, P. K. Synthesis and Characterization of Two Quaternary Thorium Chalcophosphates: $Cs_4Th_2P_6S_{18}$ and $Rb_7Th_2P_6Se_{21}$. *Inorg. Chem.* **2005**, *44* (6), 2106–2113. https://doi.org/10.1021/ic049101e.

(25) Schoop, L. M.; Eger, R.; Nuss, J.; Pielnhofer, F.; Lotsch, B. V. The First Quinary Rare Earth Thiophosphates: $Cs_5Ln_3X_3(P_2S_6)_2(PS_4)$ (*Ln* = La, Ce, *X* = Br, Cl) and the Quasi-Quaternary $Cs_{10}Y_4Cl_{10}(P_2S_6)_3$: The First Quinary Rare Earth Thiophosphates: $Cs_5Ln_3X_3(P_2S_6)_2(PS_4)$ (*Ln* = La, Ce, *X* = Br, Cl) and the Quasi-Quaternary $Cs_{10}Y_4Cl_{10}(P_2S_6)_3$. *Z. Anorg. Allg. Chem.* **2017**, *643* (23), 1818–1823. https://doi.org/10.1002/zaac.201700309.

(26) Brockner, W.; Becker, R.; Eisenmann, B.; Schäfer, H. Kristallstruktur und Schwingungsspektren der Caesium- und Kalium-Hexathiometadiphosphate $Cs_2P_2S_6$ und $K_2P_2S_6$. *Z. Anorg. Allg. Chem.* **1985**, *520* (1), 51–58. https://doi.org/10.1002/zaac.19855200107.

(27) Kuhn, A.; Eger, R.; Nuss, J.; Lotsch, B. V. Synthesis and Structural Characterization of the Alkali Thiophosphates $Na_2P_2S_6$, $Na_4P_2S_6$, $K_4P_2S_6$, and $Rb_4P_2S_6$: Alkali Thiophosphates $Na_2P_2S_6$, $Na_4P_2S_6$, $K_4P_2S_6$, and $Rb_4P_2S_6$. *Z. Anorg. Allg. Chem.* **2014**, *640* (5), 689–692. https://doi.org/10.1002/zaac.201300575.

(28) Aitken, J. A.; Canlas, C.; Weliky, D. P.; Kanatzidis, M. G. $[P_2S_{10}]^{4-}$: A Novel Polythiophosphate Anion Containing a Tetrasulfide Fragment. *Inorg. Chem.* **2001**, *40* (25), 6496–6498. https://doi.org/10.1021/ic010664p.

(29) Rothenberger, A.; Morris, C.; Kanatzidis, M. G. Synthesis of Alkali Metal Indium Thiophosphates Containing the Discrete Anions $[In(PS_4)(PS_5)_2]^{6-}$ and $[In(PS_4)_2(PS_5)]^{6-}$. *Inorg. Chem.* **2010**, *49* (12), 5598–5602. https://doi.org/10.1021/ic100495b.

(30) Alahmari, F.; Davaasuren, B.; Khanderi, J.; Rothenberger, A. Synthesis and Characterization of the Rubidium Thiophosphate $Rb_6(PS_5)(P_2S_{10})$ and the Rubidium Silver Thiophosphates Rb_2AgPS_4, $RbAg_5(PS_4)_2$ and $Rb_3Ag_9(PS_4)_4$. *Z. Anorg. Allg. Chem.* **2016**, *642* (5), 361–367. https://doi.org/10.1002/zaac.201500793.

(31) Klepov, V. V.; Pace, K. A.; Breton, L. S.; Kocevski, V.; Besmann, T. M.; zur Loye, H.-C. Nearly Identical but Not Isotypic: Influence of Lanthanide Contraction on $Cs_2NaLn(PS_4)_2$ (*Ln* = La–Nd, Sm, and Gd–Ho). *Inorg. Chem.* **2020**, *59* (3), 1905–1916. https://doi.org/10.1021/acs.inorgchem.9b03200.

(32) Sotelo, P.; Orr, M.; Galante, M. T.; Hossain, M. K.; Firouzan, F.; Vali, A.; Li, J.; Subramanian, M.; Longo, C.; Rajeshwar, K.; Macaluso, R. T. Ternary Rare Earth Sulfide CaCe2S4: Synthesis and Characterization of Stability, Structure, and Photoelectrochemical Properties in Aqueous Media. *Journal of Solid State Chemistry* **2018**, *262*, 149–155. https://doi.org/10.1016/j.jssc.2018.02.014.

(33) Li, H.; Langer, E. M.; Kegler, P.; Modolo, G.; Alekseev, E. V. Formation of Open Framework Uranium Germanates: The Influence of Mixed Molten Flux and Charge Density Dependence in U-Silicate and U-Germanate Families. *Inorg. Chem.* **2018**, *57* (17), 11201–11216. https://doi.org/10.1021/acs.inorgchem.8b01781.

(34) Li, H.; Langer, E. M.; Kegler, P.; Alekseev, E. V. Structural and Spectroscopic Investigation of Novel 2D and 3D Uranium Oxo-Silicates/Germanates and Some Statistical Aspects of Uranyl Coordination in Oxo-Salts. *Inorg. Chem.* **2019**, *58* (15), 10333–10345. https://doi.org/10.1021/acs.inorgchem.9b01523.

(35) Juillerat, C. A.; Klepov, V. V.; Morrison, G.; Pace, K. A.; Zur Loye, H.-C. Flux Crystal Growth: A Versatile Technique to Reveal the Crystal Chemistry of Complex Uranium Oxides. *Dalton Trans.* **2019**, *48* (10), 3162–3181. https://doi.org/10.1039/c8dt04675a.

(36) Li, H.; Kegler, P.; Alekseev, E. V. Crystal Growth of Novel 3D Skeleton Uranyl Germanium Complexes: Influence of Synthetic Conditions on Crystal Structures. *Dalton Trans.* **2020**, *49* (7), 2244–2257. https://doi.org/10.1039/C9DT04750F.

(37) Klepov, V. V.; zur Loye, H.-C. Complex Topologies from Simple Building Blocks: Uranium(IV) Thiophosphates. *Inorg. Chem.* **2018**, *57* (17), 11175–11183. https://doi.org/10.1021/acs.inorgchem.8b01733.

(38) Klepov, V. V.; Smith, M. D.; zur Loye, H.-C. Targeted Synthesis of Uranium(IV) Thiosilicates. *Inorg. Chem.* **2019**, *58* (13), 8275–8278. https://doi.org/10.1021/acs.inorgchem.9b01307.

(39) Klepov, V.; Juillerat, C. A.; Pace, K. A.; Morrison, G.; zur Loye, H.-C. "Soft" Alkali Bromide and Iodide Fluxes for Crystal Growth. *Front. Chem.* **2020**. https://doi.org/10.3389/fchem.2020.00518.

(40) Komm, T.; Gudat, D.; Schleid, T. The $M[PS_4]$-Type Lanthanide(III) Ortho-Thiophosphates(V) (M = La–Nd, Sm, Gd–Er): Synthesis, Crystal Structure, and ^{31}P NMR Investigations. *Z. Naturforsch. B* **2006**, *61* (6), 766–774. https://doi.org/10.1515/znb-2006-0618.

(41) Ohta, M.; Hirai, S.; Kato, H.; Sokolov, V. V.; Bakovets, V. V. Thermal Decomposition of NH_4SCN for Preparation of Ln_2S_3 (Ln = La and Gd) by Sulfurization. *Mater. Trans.* **2009**, *50* (7), 1885–1889. https://doi.org/10.2320/matertrans.M2009060.

(42) Hadenfeldt, C.; Hoedel, D. Kristallstruktur und Eigenschaften von Calcium- und Strontiumhexathiodiphosphat(IV), $Ca_2P_2S_6$ und $Sr_2P_2S_6$, mit einem Beitrag zu Ca_5P_8 und $Pb_2P_2S_6$. *Z. Anorg. Allg. Chem.* **1996**, *622* (9), 1495–1500. https://doi.org/10.1002/zaac.19966220910.

(43) *SAINT*; Bruker AXS Inc.: Madison, Wisconsin, USA, 2012.

(44) Krause, L.; Herbst-Irmer, R.; Sheldrick, G. M.; Stalke, D. Comparison of Silver and Molybdenum Microfocus X-Ray Sources for Single-Crystal Structure Determination. *J. Appl. Cryst.* **2015**, *48* (1), 3–10. https://doi.org/10.1107/S1600576714022985.

(45) Dolomanov, O. V.; Bourhis, L. J.; Gildea, R. J.; Howard, J. A. K.; Puschmann, H. OLEX2: A Complete Structure Solution, Refinement and Analysis Program. *J. Appl. Cryst.* **2009**, *42* (2), 339–341.

(46) Sheldrick, G. M. Crystal Structure Refinement with *SHELXL*. *Acta Crystallogr. C Structural Chemistry* **2015**, *71* (1), 3–8. https://doi.org/10.1107/S2053229614024218.
(47) Spek, A. Structure Validation in Chemical Crystallography. *Acta Crystallogr. D* **2009**, *65* (2), 148–155.
(48) Morrison, G.; zur Loye, H.-C. Simple Correction for the Sample Shape and Radial Offset Effects on SQUID Magnetometers: Magnetic Measurements on Ln_2O_3 (*Ln* = Gd, Dy, Er) Standards. *J. Solid State Chem.* **2015**, *221*, 334–337. https://doi.org/10.1016/j.jssc.2014.10.026.
(49) Blatov, V. A.; Shevchenko, A. P.; Serezhkin, V. N. *TOPOS* 3.2: A New Version of the Program Package for Multipurpose Crystal-Chemical Analysis. *J. Appl. Cryst.* **2000**, *33* (4), 1193–1193. https://doi.org/10.1107/S0021889800007202.
(50) Blatov, V. A. Multipurpose Crystallochemical Analysis with the Program Package TOPOS. *IUCr CompComm Newslett.* **2006**, *7*, 4.
(51) Blatov, V. A.; Serezhkin, V. N. Stereoatomic Model of the Structure of Inorganic and Coordination Compounds. *Russ. J. Inorg. Chem.* **2000**, *45*, S105–S222.
(52) Blatov, V. A.; Shevchenko, A. P.; Proserpio, D. M. Applied Topological Analysis of Crystal Structures with the Program Package ToposPro. *Cryst. Growth Des.* **2014**, *14* (7), 3576–3586. https://doi.org/10.1021/cg500498k.
(53) Kresse, G.; Furthmüller, J. Efficiency of Ab-Initio Total Energy Calculations for Metals and Semiconductors Using a Plane-Wave Basis Set. *Computational Materials Science* **1996**, *6* (1), 15–50. https://doi.org/10.1016/0927-0256(96)00008-0.
(54) Kresse, G.; Furthmüller, J. Efficient Iterative Schemes for *Ab Initio* Total-Energy Calculations Using a Plane-Wave Basis Set. *Physical Review B* **1996**, *54* (16), 11169–11186. https://doi.org/10.1103/PhysRevB.54.11169.
(55) Perdew, J. P.; Burke, K.; Ernzerhof, M. Generalized Gradient Approximation Made Simple. *Physical Review Letters* **1996**, *77* (18), 3865–3868. https://doi.org/10.1103/PhysRevLett.77.3865.
(56) Blöchl, P. E. Projector Augmented-Wave Method. *Physical Review B* **1994**, *50* (24), 17953–17979. https://doi.org/10.1103/PhysRevB.50.17953.
(57) Kresse, G.; Joubert, D. From Ultrasoft Pseudopotentials to the Projector Augmented-Wave Method. *Physical Review B* **1999**, *59* (3), 1758–1775. https://doi.org/10.1103/PhysRevB.59.1758.
(58) Yao, J.; Ibers, J. A. $RbPbPS_4$. *Acta Crystallogr. E Struct Rep Online* **2004**, *60* (9), i108–i110. https://doi.org/10.1107/S1600536804018513.
(59) Komm, T.; Strobel, S.; Schleid, T. Two Potassium Gadolinium(III) Ortho-Thiophosphates(V): $K_3Gd_3[PS_4]_4$ and $K_9Gd[PS_4]_4$. *J. All. Comp.* **2008**, *451* (1–2), 648–653. https://doi.org/10.1016/j.jallcom.2007.04.080.
(60) Mesbah, A.; Prakash, J.; Rocca, D.; Lebègue, S.; Beard, J. C.; Lewis, B. A.; Ibers, J. A. Syntheses, Crystal Structure, and Electronic Properties of the Five $ABaMQ_4$ Compounds $RbBaPS_4$, $CsBaPS_4$, $CsBaVS_4$, $RbBaVSe_4$, and $CsBaVSe_4$. *J. Solid State Chem.* **2016**, *233*, 217–220. https://doi.org/10.1016/j.jssc.2015.10.028.
(61) Xiao, B.; Schlenz, H.; Dellen, J.; Bosbach, D.; Suleimanov, E. V.; Alekseev, E. V. From Two-Dimensional Layers to Three-Dimensional Frameworks: Expanding the Structural Diversity of Uranyl Compounds by Cation–Cation Interactions. *Cryst. Growth Des.* **2015**, *15* (8), 3775–3784. https://doi.org/10.1021/acs.cgd.5b00427.
(62) Alekseev, E. V.; Krivovichev, S. V.; Armbruster, T.; Depmeier, W.; Suleimanov, E. V.; Chuprunov, E. V.; Golubev, A. V. Dimensional Reduction in Alkali Metal Uranyl Molybdates: Synthesis and Structure of $Cs_2[(UO_2)O(MoO_4)]$. *Z. Anorg. Allg. Chem.* **2007**, *633* (11–12), 1979–1984. https://doi.org/10.1002/zaac.200700270.
(63) Schoop, L. M.; Eger, R.; Kremer, R. K.; Kuhn, A.; Nuss, J.; Lotsch, B. V. Structural Stability Diagram of $ALnP_2S_6$ Compounds (A = Na, K, Rb, Cs; Ln = Lanthanide). *Inorg. Chem.* **2017**, *56* (3), 1121–1131. https://doi.org/10.1021/acs.inorgchem.6b02052.
(64) Gauthier, G.; Jobic, S.; Evain, M.; Koo, H.-J.; Whangbo, M.-H.; Fouassier, C.; Brec, R. Syntheses, Structures, and Optical Properties of Yellow Ce_2SiS_5, $Ce_6Si_4S_{17}$, and $Ce_4Si_3S_{12}$ Materials. *Chem. Mat.* **2003**, *15* (4), 828–837. https://doi.org/10.1021/cm0211711.

For Table of Contents use only

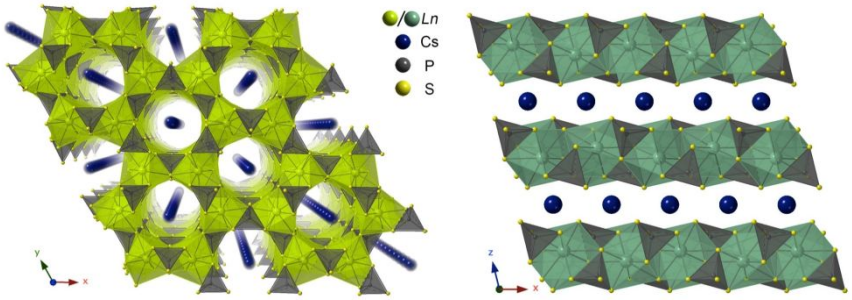

A series of Ca-containing lanthanide thiophosphates has been obtained and their structural evolution from 3D for LnPS$_4$ and Cs$_{0.3}$($Ln_{0.7}$Ca$_{0.3}$)PS$_4$ to 2D in Cs$_{0.5}$($Ln_{0.5}$Ca$_{0.5}$)PS$_4$ was shown as a function of Ca content.